

See discussions, stats, and author profiles for this publication at: <https://www.researchgate.net/publication/263980313>

Direct Evidence of Chemically Inhomogeneous, Nanostructured, Si–O Buried Interfaces and Their Effect on the Efficiency of Carbon Nanotube/Si Photovoltaic Heterojunctions

ARTICLE in THE JOURNAL OF PHYSICAL CHEMISTRY C · AUGUST 2013

Impact Factor: 4.77 · DOI: 10.1021/jp404820k

CITATIONS

7

READS

54

10 AUTHORS, INCLUDING:



Stefania Pagliara

Catholic University of the Sacred Heart

67 PUBLICATIONS 495 CITATIONS

SEE PROFILE



Luigi Sangaletti

Catholic University of the Sacred Heart

174 PUBLICATIONS 2,164 CITATIONS

SEE PROFILE



Maurizio De Crescenzi

University of Rome Tor Vergata

263 PUBLICATIONS 3,803 CITATIONS

SEE PROFILE



Paola Castrucci

University of Rome Tor Vergata

124 PUBLICATIONS 1,391 CITATIONS

SEE PROFILE

Direct Evidence of Chemically Inhomogeneous, Nanostructured, Si–O Buried Interfaces and Their Effect on the Efficiency of Carbon Nanotube/Si Photovoltaic Heterojunctions

Chiara Pintossi,[†] Gabriele Salvinelli,[†] Giovanni Drera,[†] Stefania Pagliara,[†] Luigi Sangaletti,^{*,†} Silvano Del Gobbo,[‡] Maurizio Morbidoni,[§] Manuela Scarselli,[§] Maurizio De Crescenzi,[§] and Paola Castrucci[§]

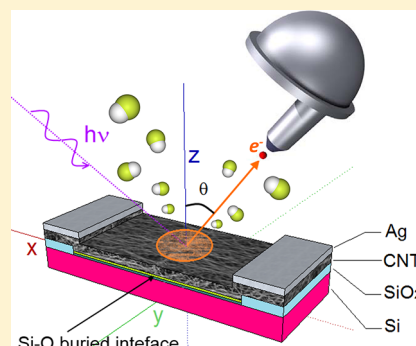
[†]Interdisciplinary Laboratories for Advanced Materials Physics (I-LAMP) and Dipartimento di Matematica e Fisica, Università Cattolica del Sacro Cuore, I-25121 Brescia, Italy

[‡]King Abdullah University of Science & Technology, Thuwal 23955, Kingdom of Saudi Arabia

[§]Unità CNISM and Dipartimento di Fisica, Università di Roma Tor Vergata, I-00133 Roma, Italy

Supporting Information

ABSTRACT: An angle resolved X-ray photoemission study of carbon nanotube/silicon hybrid photovoltaic (PV) cells is reported, providing a direct probe of a chemically inhomogeneous, Si–O buried interface between the carbon nanotube (CNT) networked layer and the n-type Si substrate. By changing the photoelectron takeoff angle of the analyzer, a nondestructive in-depth profiling of a CNT/SiO_x/SiO₂/Si complex interface is achieved. Data are interpreted on the basis of an extensive modeling of the photoemission process from layered structures, which fully accounts for the depth distribution function of the photoemitted electrons. As X-ray photoemission spectroscopy provides direct access to the buried interface, the aging and the effects of chemical etching on the buried interface have been highlighted. This allowed us to show how the thickness and the composition of the buried interface can be related to the efficiency of the PV cell. The results clearly indicate that while SiO₂ is related to an increase of the efficiency, acting as a buffer layer, SiO_x is detrimental to cell performances, though it can be selectively removed by etching in HF vapors.



■ INTRODUCTION

The peculiar mechanical and electronic properties¹ of carbon nanotubes (CNTs) have attracted a growing interest for nanotechnological applications. Among different types of CNTs, single-walled carbon nanotubes (SWCNTs) exhibit a metallic or semiconducting behavior depending on their chirality, while their density of states presents van Hove singularities that allow optical transitions ranging from the infrared to the near-ultraviolet.² Theoretical studies³ have predicted photoconductivity of individual tubes, and appreciable photocurrent was observed when nanotube films were irradiated with light.^{4,5} Because of these characteristics, several different CNT-based photovoltaic devices have been fabricated. In these applications, carbon nanotubes have been used directly as photoactive material^{6,7} or most often as simply nanoscale fillers (providing additional transport paths) in the polymer matrix of organic solar cells^{8,9} or as transparent electrodes for collecting charge carriers.^{10,11}

In the last cited studies, nanotubes do not participate in the photogeneration process because excitons are generated mainly in the conjugated polymers, whereas the nanotubes, embedded into the polymer matrix, only provide more interfacial area for exciton dissociation and charge transport path. All these cells

have shown a rather low efficiency (about 0.1%), even with the addition of sensitizing dyes. As recently reported,^{12–16} higher efficiencies (about 11–13%) can be achieved by building hybrid photovoltaic devices, based on SWCNT/Si heterojunctions. For these devices, the preparation of the SWCNT film plays a key role. In the present work, a film made of a highly entangled self-sustaining network of SWCNT is cast on a cellulose membrane surface and then transferred onto the silicon substrate resulting in a hybrid Si-CNT heterojunction. The intimate contact gives rise to the formation of multiple junctions at the interface with Si and to the build-up of an electric field that can split charge carriers (e–h), under illumination, in the Si layer. The SWCNT film itself works as a transport path for charge carriers (holes), while the n-type silicon wafer, used to extract electrons, is the main photogeneration site from which electrons are collected through an ohmic junction with the metal contact underneath.¹⁵ In this kind of device, the SWCNT film thickness plays a double role: it should allow the largest number of photons to reach the Si

Received: May 16, 2013

Revised: July 22, 2013

Published: August 12, 2013



layer, and, at the same time, it must be conductive enough to allow charge transport without significant losses. It was also claimed¹² that oxide-free Si surfaces favor the formation of more efficient heterojunctions with CNTs. As devices are prepared in air, it appears appropriate to investigate if the presence of any oxide influences the formation and the behavior of the junction. Speculations about the role of a silicon oxide layer on the cell efficiency have been proposed,^{12,17} but direct evidence of this layer and its physical and chemical characteristics (thickness, homogeneity, chemical composition) has not yet been reported.

The aim of the present study is to investigate by angle-resolved X-ray photoemission spectroscopy (AR-XPS) the electronic properties of the buried interfaces in the hybrid CNT/Si heterojunction and their effect on the overall efficiency of the devices. This is accomplished by an extensive modeling of the complex CNT/SiO_x/SiO₂/Si heterostructure which also provided important details on the thickness of each layer, along with an indication of partial coverage of the surface. Incidentally, we show that AR-XPS is an excellent tool for nondestructive depth profiling of nanostructured devices. We have been able to show that the thickness and the chemical composition of the buried interface can determine the efficiency of the photovoltaic (PV) cell. In particular, we show that XPS can provide straightforward information about changes in the Si–O layer resulting from etching effects aimed to control the thickness of the buried silicon oxide interface.

EXPERIMENTAL AND COMPUTATIONAL DETAILS

Device Manufacturing. The substrates, provided by FBK (Fondazione Bruno Kessler, Trento, Italy), consisted of 5×10 mm² slices of a SiO₂ passivated (thickness 300 nm) n-type Si(100), resistivity $3\text{--}12 \Omega \times \text{cm}$ with an aluminum ohmic back contact. The oxide layer was patterned by a lithographic process with a positive resist followed by a chemical etching in order to obtain a 5×5 mm² bare silicon window delimited aside by two SiO₂ steps. Therefore, the device active area is 5×5 mm². The chemical etching was carried out by wetting for 5 min the bare SiO₂ by a HF/NH₄F buffer solution.

Networked SWCNT films were obtained from SWCNT powders (sample A: metallic SWCNT, $d = 0.7\text{--}1.4$ nm, carbon $>90\%$, purity $\geq 77\%$, density 0.09 g/cm^3 ; samples B and C: semiconducting SWCNT (6,5) chirality, carbon $>90\%$, purity $\geq 77\%$, $d = 0.7\text{--}0.9$ nm, density 0.14 g/cm^3) both provided by Sigma-Aldrich. For the deposition of the SWCNT film onto the Si patterned substrates, a SWCNT dispersion was prepared by ultrasound treatment of $100 \mu\text{g}$ of SWCNT powder in a 3 wt % aqueous solution of sodium dodecylsulfate (SDS) (98.5% Sigma Aldrich). After 1 h of ultrasound treatment, the dispersion was left to settle down, and the clear supernatant containing unbundled nanotubes was divided from the precipitate (mostly bundled nanotubes) and used to fabricate the film. The filtration process of the SWCNT dispersion in water was carried out by a vacuum filtration assembly to speed up the process using a cellulose acetate membrane filter (PALL corp. $0.45 \mu\text{m}$ diameter pores).

Once the SWCNT film was cast on the membrane filter, the residual SDS was removed by washing with deionized water and subsequently by an ethanol/methanol/water mixture (15:15:70 in volume). Films with different thickness were obtained by filtering different aliquots in volume of the same solution. The SWCNT film was transferred on the patterned Si substrate flipping it over and pressing the SWCNT coated

membrane onto the Si/SiO₂ surface. To improve the adhesion and to promote the SWCNT film detachment from the membrane, this latter is soaked with ethanol and subsequently dried under a vacuum. The residual cellulose acetate membrane lying on top of SWCNT film is removed by dipping the entire sample in warm acetone (30°C) 3–4 times and finally rinsing in isopropanol. Finally, two silver painted metallic contacts are created on the SWCNT film just on top of the SiO₂ steps. The presence of SiO₂ steps between the metal electrodes and the Si underneath is fundamental to avoid short-circuits causing electron leakage. A scheme of the device is reported in Figure 1. The samples considered in this study are listed below:

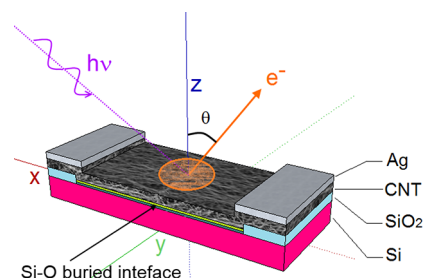


Figure 1. Schematic drawing of the CNT-Si hybrid heterojunction and representation of the XPS experimental geometry. The angle θ between the direction of the outgoing electron and the z axis is the photoelectron takeoff angle, which is referred to in the angle-resolved measurements.

- Samples A and B: both substrates were prepared in a single batch and exposed to air for several days prior to the SWCNT film transfer;
- Sample C: nanotubes were transferred on the substrate as soon as the Si substrate was prepared.

The sheet resistance and the optical transmittance measured at 550 nm for the three samples are reported in Table 1. Further details on the optical characterization are reported in the Supporting Information file.

Efficiency Measurements. The PV efficiency measurements were carried out using a solar simulator Oriel LSO106 equipped with a 150 W Xe lamp, an AM1.5 global filter, and a Keithley sourcemeter 6202A. The devices were connected to the sourcemeter according to this scheme: Al contact on Si - ground, SWCNT film - signal. The results in term of efficiency derived from I/V curves are reported in Table 1. $I-V$ curves measured after etching of the whole junction were collected with an halogen lamp and a custom-made $I-V$ tracker, driven by a National Instrument PCIe-6251 data acquisition board through the LABview software package.

XPS Measurements. The XPS data have been collected at the Surface Science and Spectroscopy Lab of the Università Cattolica del Sacro Cuore (Brescia, Italy) with a SCIENTA R3000 electron spectrometer, operating in the transmission mode and working with a 30° acceptance angle. The Al K _{α} line ($h\nu = 1486.6$ eV, resolution 0.85 eV) of a non-monochromatized dual-anode PsP X-ray source was used, running at a power of about 110 W. The base pressure in the sample analysis chamber was 2×10^{-10} mbar. With the sample holder clips being coated with gold, the binding energy (BE) of the Au 4f_{7/2} peak (BE = 83.96 eV)¹⁸ was taken as a reference.

In the present study, the analyzer transmission (or large acceptance) mode has been employed to maximize the count ratio and, thus, to speed up the acquisition time while keeping

Table 1. Main Properties of the SWNTs and PV Cells

sample	type	quantity of CNTs (mL)	efficiency η (%)	sheet resistance (k Ω)	optical transmittance at $\lambda = 550$ nm (%)
A	metallic	1.5	0.26	2.4	64.0
B	semiconductor	2.0	0.20	1.8	66.0
C	semiconductor	3.5	2.72	0.4	65.0

the energy resolution required for a reliable peak fitting. Because of the large thickness of CNT overlayer and the weakness of XPS signal from silicon, any improvement of the signal-to-noise ratio has been fundamental. The effect of the analyzer angular acceptance on XPS measurement is usually weak, especially when (as in the present case) the angle between the source and the analyzer axis is close to the “magic angle” (54.5°) and when the tilt angle is lower than 70° . Waligorski and Cooke¹⁹ have shown that a large acceptance can improve the signal-to-noise ratio without reducing the effectiveness with which the detector can measure the angular distribution.

ARXPS calculations of the C 1s and Si 2p peak areas carried out with the DDF approach for a CNT/silicon interface (see Figure 2 in the Supporting Information) indicate that discrepancies between the C 1s and Si 2p relative intensities are kept below about 5% in the whole θ -range considered (0 – 60°). Since in ref 20, it has been shown that deviation from the predicted behavior can be found for takeoff angles θ above 70° , in the present study the maximum takeoff angle of all experiments is limited to 50° .

Modeling of AR-XPS. Modeling and simulation of the multilayer structure, aimed to fit the XPS peak angular dependence, was carried out with code developed at the Surface Science and Spectroscopy Lab, based on the IGOR 6.3 programming language. A variety of physical processes are known to play an important role in the XPS signal generation, such as elastic and inelastic scattering in the interior of the solid, surface excitations, and intrinsic excitations following the ionization that precedes the signal electron emission in XPS. Generally, such processes can occur repeatedly (multiple scattering) before the electron is ejected from the surface, giving rise to a complex combination of effects responsible for some important features observed in experimental spectra. In XPS, the core-level peak intensities $I(E_k, \theta)$ of a selected layer at a depth d with a thickness t can be evaluated through the formula:

$$I(E_k, \theta) = N \cdot X_s \int_d^{d+t} \text{DDF}(E_k, \theta, z) dz$$

where N is the atomic density of the involved species, and X_s represents the photoionization cross section,²¹ depending also on the analyzer geometry; $\text{DDF}(E_k, \theta, z)$ is the escape probability, known as depth distribution function, of an electron generated at a depth z with a kinetic energy E_k at an angle θ , with respect to the surface normal (Figure 1). According to the Lambert–Beer law, the DDF function is usually approximated with a Poisson distribution $\Phi = \exp(-z/\lambda \cos \theta)$,²² where λ is the inelastic mean free path (IMFP).²³ When the direction of detection is along the normal to the surface ($\theta = 0$), the average depth of the sample being analyzed will then be $<3\lambda$, but if one records a signal at an angle $\theta > 0$ with respect to the surface, the sampled thickness is reduced to $\sim 3\lambda \cos \theta$. In this work, following ref 24, we used Monte Carlo DDF calculations, including inelastic and elastic electronic scattering, in the transport approximation. The photoemission

asymmetry parameters have been taken into account for each core-level. Monte Carlo calculations of electron trajectories have been carried out in order to predict the XPS peak intensities from each layer in our heterostructures.

Raman Measurements. Raman spectra have been collected with a Renishaw spectrometer equipped with a He–Ne laser ($\lambda = 632.8$ nm) and a Leika confocal microscope. A $50\times$ microscope objective (N.A. = 0.75) has been used to collect the inelastically scattered light in a backscattering geometry. The laser power on the sample was 1.4 mW.

RESULTS AND DISCUSSION

Carbon 1s Core Levels. In Figure 2, the C 1s XPS core levels of the three samples are shown. An asymmetric peak with

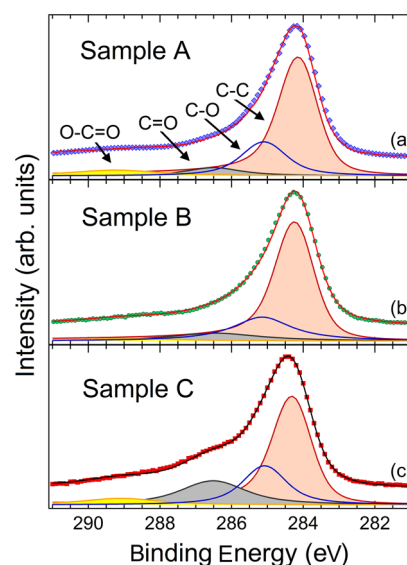


Figure 2. C 1s XPS core level data, and fitting with 4 components related to the C–C, C–O, C=O, and O–C=O bonds. Panels a, b, and c refer to samples A, B and C, respectively. All spectra have been normalized to the maximum of the C 1s peak at 284.5 eV.

maximum at a binding energy (BE) of 284.5 eV is detectable, with a tail on the high BE side, ranging up to 292 eV. Panels a, b, and c refer to the data of samples A, B, and C, respectively. For a more detailed analysis of the C 1s lineshapes, we resorted to a data fitting aimed to identify the different carbon bonds contributing to each spectrum, along with their relative weight. The fitting results for the C 1s photoemission peaks are also shown in Figure 2.

For the main peak at 284.5 eV, due to the contribution of the C–C bond, the peak fitting is carried out on the basis of the Doniach–Sunjic²⁵ line shape, as is usually done for CNTs.²⁶ In all these fits, we use a fixed value for the asymmetry parameter α of the carbon peak ($\alpha = 0.075$), as reported in the literature for graphene sheets.²⁷ In the peak fitting, we considered the possible contributions of four peaks ascribed to the C–C, C–O, C=O, and O–C=O bonds.²⁸

In the fitting procedure, the binding energy of each peak has been kept fixed, according to the values available in the literature,²⁸ while the full width at half-maximum (fwhm) and the intensity were used as parameters in the fitting. The fwhm difference among similar peaks in the three samples was allowed to vary within $\pm 10\%$, assuming that these differences could be ascribed to the different environment where the specific carbon–oxygen bonds (C–O, C=O, and O–C=O) could be found, i.e., in the CNT bundles, at the surface, or at the CNT–SiO_x interface. For each sample, the relative weights of the four peaks are reported in Table 2.

Table 2. Results of the Analysis of the C 1s XPS Peak

sample	C–C (%)	C–O (%)	C=O (%)	O–C=O (%)
A	65.2	20.7	6.3	7.8
B	65.8	21.1	9.9	3.2
C	53.7	21.7	19.0	5.6

As can be seen in Table 2, most of the C 1s spectral weight comes from the C–C bond (about 60%), while the remaining weight is ascribed to single and double bonds between carbon and oxygen. Within the accuracy of the fitting procedure, we can assume that the three samples do not present significant differences among the main components. This justifies our choice to normalize all the ARXPS spectra to the C 1s core level intensity, collected at a takeoff angle $\theta = 0^\circ$ between the analyzer and the normal to the sample surface.

Silicon 2p Core Levels. Figure 3 shows the Si 2p core levels of the three samples collected at different takeoff angles in the 0 – 50° range. Results from sample A, B, and C are shown in the left, central, and right panels, respectively. As can be observed, two main peaks corresponding to bulk silicon (BE = 99.5 eV) and to the SiO₂ native oxidation layer (BE = 103.2 eV) contribute to the spectral weight. On the basis of the binding energies alone, the central peak could be ascribed both to the silicon carbide SiC (with a BEs reported in the range from 99.85 eV²⁹ to 100.8 eV³⁰) and to the nonstoichiometric silicon oxide SiO_x (BE from 100.4 to 103.23 eV).²⁰

We exclude silicon carbide as the origin of the middle peak, as we did not observe its counterpart in the C 1s spectral region. Indeed, in silicon carbide a C 1s peak at 282.5 eV is expected, as reported in ref 31, but this peak is absent in all samples here considered. Therefore, we are able to conclude that the central peak is due to SiO_x.

The three peaks so far identified show a distinct angular dependence as the analyzer takeoff angle θ is swept from the normal emission geometry (0°) to a more grazing emission angle (50°). In particular, we observe a steep decrease of the Si bulk signal as the probe is getting more surface sensitive, a roughly constant behavior of SiO_x, and a weak decrease of the SiO₂ contribution. As expected, this behavior agrees with the sequence of layers of the heterostructure. Silicon is the deepest layer, while SiO₂ and SiO_x lay in-between silicon and the CNT topmost layer.

In Figure 3, the fitting results for the angle resolved Si 2p photoemission peak are also shown. All peaks are fitted by

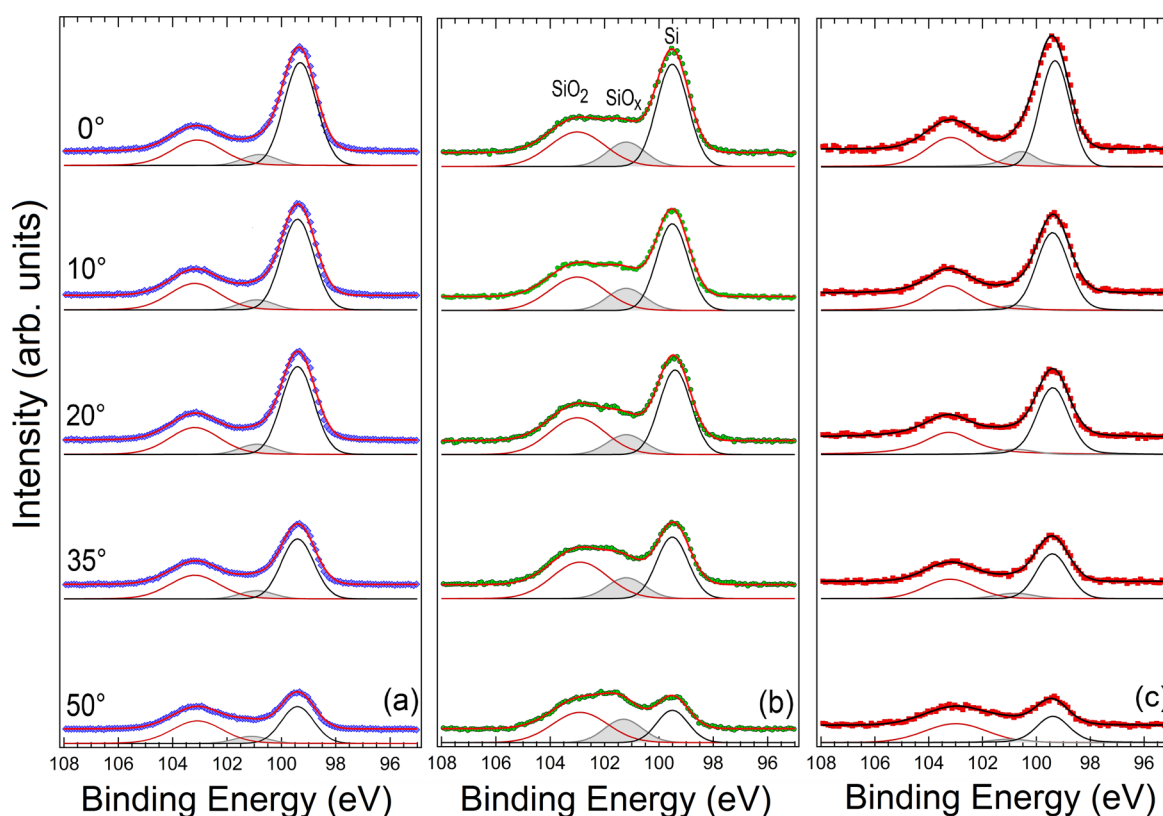


Figure 3. AR-XPS results for the silicon 2p peaks, normalized to C 1s intensity (left panel: sample A, central panel: sample B, right panel: sample C). The takeoff angles θ (see Figure 1) between the normal to the surface and the detector vary between 0° and 50° and are reported on the left panel. The red component at high binding energy is ascribed to SiO₂, the midenergy, filled gray peak is ascribed to SiO_x, while the black component at low binding energy is ascribed to the bulk n-doped silicon.

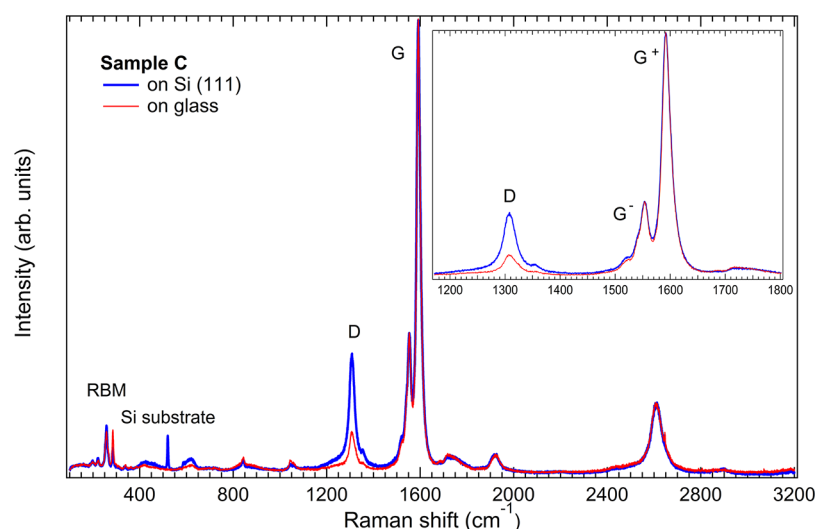


Figure 4. Raman spectra for sample C (thick blue line) and its counterpart on glass (thin red line). Inset: enlarged view of the spectral region where the D and G bands are detectable.

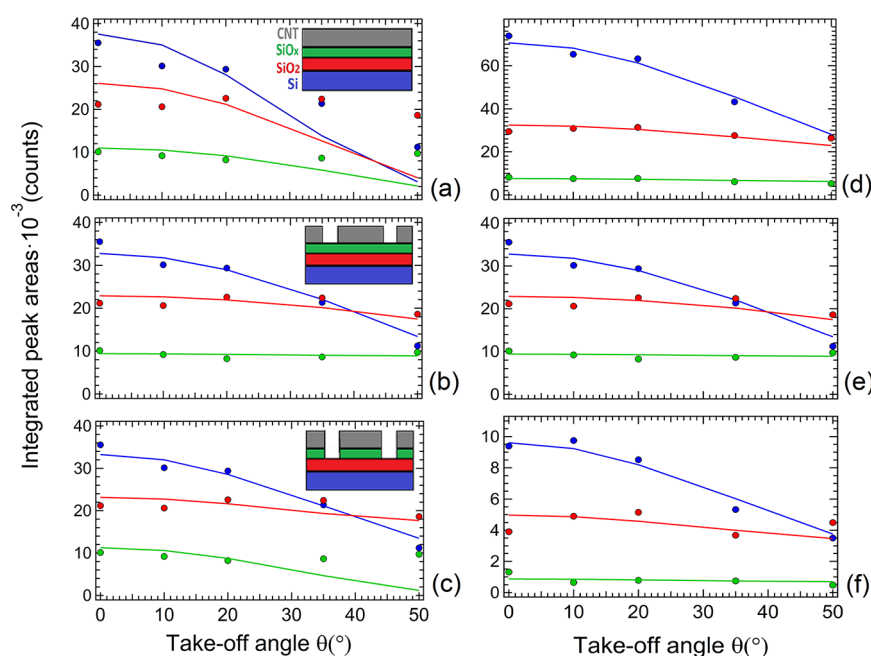


Figure 5. Dependence of the Si, SiO₂, and SiO_x XPS integrated peak areas on the takeoff angle θ . The lines are drawn according to the Global fit results, based on different models for the stacking of layers. Left panel: effects of the island distribution on the model output. The AR-XPS data are those extracted from the angle-resolved spectra of sample B. (a) No island; (b) island in the CNT film alone; (c) island extended to the SiO_x layer. For all samples, the model that best matches the AR-XPS data is the second (b). Right panel: (d–f) AR-XPS data and global fit results for samples A, B, and C, with an island only in the CNT layer.

using Voigt functions. It is important to observe that the SiO_x peak was not detected in the CNT-free substrate prior to the transfer of the CNT film (spectra not shown here), so its presence should be related to CNTs. The SiO_x layer may be in fact originated by the action of chemicals used to treat and transfer the CNT film or by a direct interaction between nanotubes and the native SiO₂ oxide layer. It is known³² that, by pouring sulfur-based solutions (such as Piranha solution and SDS) on a silicon crystal, it is possible to obtain a layer of SiO_x. Piranha solution is a very strong oxidizer which first removes organic particles and deposited contaminants and then removes covalently adhered oxygen molecules, replacing them with hydrophilic OH molecules. On the other hand, because of

strong van der Waals forces, upon CNT deposition, the oxygen atoms of SiO₂ can be pulled toward the nanotubes, yielding a thin layer of amorphous SiO_x. This passivation layer has a dangling bond defect density that is about 2 orders of magnitude higher than that of thermal oxides.³³

In order to test these assumptions, the CNTs used in the preparation of sample C have been also transferred on glass, and Raman spectroscopy measurements on these two samples have been carried out. The resulting spectra are shown in Figure 4. It is possible to discriminate the sample transferred on glass because of the absence of the characteristic first-order Raman line for a silicon crystal at 520 cm⁻¹.

Table 3. Results of the ARXPS Data Analysis Obtained by Modeling with a CNT-SiO_x-SiO₂-Si Multilayered Structure

sample	CNTs (Å)	SiO _x (Å)	SiO ₂ (Å)	island ratio (%)	SiO _x /SiO ₂ (%)	efficiency η (%)
A	254 ± 12	3.1 ± 0.4	13.9 ± 0.4	99.83 ± 0.02	23	0.26
B	346 ± 44	6.6 ± 0.4	19.1 ± 0.6	99.75 ± 0.02	35	0.20
C	360 ± 17	2.5 ± 0.7	15.1 ± 0.7	99.98 ± 0.01	17	2.72

Since the CNTs transferred both on glass and silicon are of the same type, the radial breathing modes (RBM) are identical, but the defect bands (D) of these samples present a remarkable difference. In particular, sample C shows a more intense D-mode at 1310 cm⁻¹, when the spectra are normalized to the maximum of the G⁺ band. This can be assumed as a proof of a higher density of defects when the CNTs are deposited on the (oxidized) silicon wafer. However, at this stage it is not possible to assess the origin of SiO_x, and we cannot exclude that the following causes can occur at the same time: (i) SDS is present in the CNT dispersion. Rinsing of the sample before the membrane filtration is expected to eliminate the SDS, but the XPS survey spectra showed that traces of S and Na are still detectable in the device. The formation of SiO_x could then be related (ref 32) to the presence of residual SDS. (ii) On the other hand, the anchoring of CNTs on the SiO₂ layer can determine the formation of SiO_x (ref 33) and of the defects, detected by Raman spectroscopy, in the CNTs contacting the SiO₂ native oxide layer.

Global Fits of the AR-XPS Data. The interface modeling was carried out by considering a stack of layers with a nonuniform coverage on the topmost layers. For each takeoff angle θ , the area of all peaks (Si, SiO_x and SiO₂) contributing to the Si 2p spectral weight was considered, normalized to the C 1s peak area, and then processed using a dedicated software developed by the authors, based on algorithms written in the programming language of the IGOR Pro 6.3 software.

After the chemical composition and the density of each layer are specified, the software calculates the DDF, and it is possible to create a layered model, initially guessing the layer thickness and the covering percentage (or island ratio). The fitting algorithm is therefore aimed to reproduce the experimental data (i.e., the peak intensity dependence on the takeoff angle θ), by using as fitting parameters all the thicknesses and the island ratio of the two topmost layers. The experimental data are compared in all steps of the fitting procedure with the expected intensities, calculated on the basis of the DDF function, the analyzer transmission, and the photoemission cross section. The fitting program then yields the estimated thickness of each layer as well as the island density in the CNT and SiO_x layers.

In order to model the sequence of layers at the interface, various attempts have been made, starting from models without island (Figure 5a) to models where the island also affects deeper layers (such as SiO_x, Figure 5c). For all samples, the best result (in terms of Chi-square) was obtained by assuming island only in the CNT topmost layer, as shown in Figure 5b. In particular, by comparing panels a and b, it is clear that the possibility to have an island in the topmost (i.e., CNT) layer yields an increase of the calculated intensities of the SiO_x and SiO₂ peaks at high takeoff angles. In turn, the addition of an island in the SiO_x layer quenches too much the calculated intensity at high takeoff angles with respect to the measured angular dependence.

Finally, the best fitting results obtained for the three samples are shown in Figure 5d–f, while the thickness calculated for each layer is reported in Table 3.

The first achievement of the ARXPS modeling is to show the possibility to estimate the overall thickness of the buried Si–O interface. In the present case, the thickness ranges from about 1.7 nm (sample A) to 2.6 nm (sample B). These values are those expected for the native oxide layer covering a silicon substrate, but they are different for the three samples, the thicker layer being that of sample B, while for the A and C samples the overall thickness is comparable. For each sample, the SiO_x/SiO₂ ratio is also different, and it is worth noting that the lowest SiO_x/SiO₂ ratio (17%) is shown by the device with highest efficiency (sample C), while for sample B, the least efficient of all, the ratio is the highest (35%). Finally, the thickness of the CNT layer is similar for the B and C samples, while it is lower in sample A, roughly scaling with the amount of CNT dispersion used to prepare the CNT layer.

As stated in the Introduction, the film thickness appears to be one of the factors that affects the cell efficiency, but the present results show that the silicon oxide role is not negligible at all. In sample A, the SWCNTs are mostly metallic, but sample A shows a thinner oxide layer with respect to B, that in turn has been prepared with semiconducting SWCNTs. These factors might cooperate to provide the higher efficiency of A with respect to B. On the other hand, sample C displays the largest efficiency and an oxide layer comparable to sample A, though with a different SiO_x/SiO₂ ratio. Apparently, the 10-fold higher η of sample C can be related to a combination of advantageous parameters. First of all, sample C is characterized by being close to the CNT film thickness that is known to maximize the efficiency, as shown in a previous work;³⁴ moreover, in this sample the CNT coverage results to be the most uniform, as the density of island is the lowest among the samples. Finally, in this sample the heterojunction formation could be favored by the amount of oxides. However, such a large difference in efficiency between samples B and C cannot be explained by focusing only on the CNT film characteristics and must be necessarily related to effects at the interface.

In order to clarify the role played by the oxide in the device operation, we resorted to etch the oxide layer to track the oxidation of the interface by XPS and to monitor the cell efficiency by *I*–*V* measurements. Therefore, following ref 17, sample B was as first etched for 20 s in HF vapors in order to remove the oxide layers, and then left in air for about 300 h, to restore the native oxide layer. Any change of the electrical properties of the device was monitored through the acquisition of *I*–*V* characteristics, and, in parallel, the Si 2p peak and C 1s were analyzed via XPS, in order to ensure that changes are due to the modulation of the thickness of the oxide layer and not to other effects, such as the acid doping of CNTs.¹⁴

The effects of acid doping on CNTs are excluded at the present stage, as the line shape of the C 1s core level ascribed to the CNT contribution did not change upon etching and during the oxidation in air (not shown here). In turn, major changes were observed in the buried interface. In Figure 6a, the Si2p

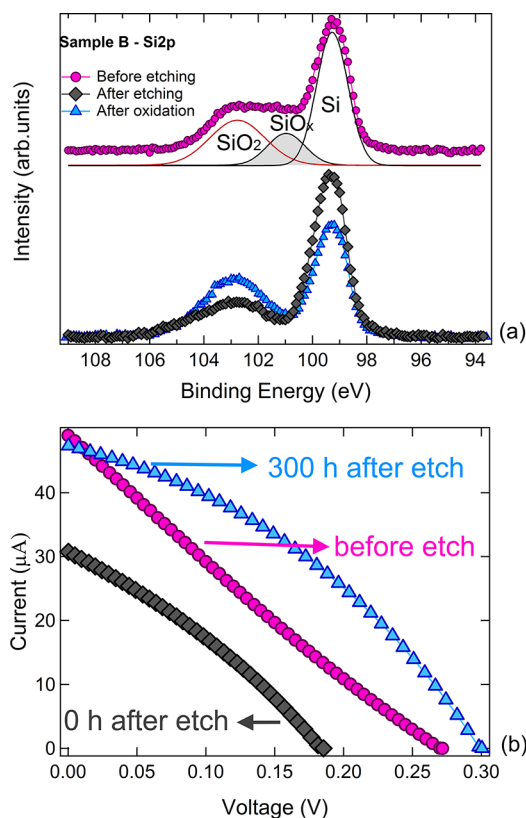


Figure 6. Etching effects on electronic and PV properties of sample B; the sample before the etching is represented with pink circles, after the etching with black diamonds, and after the oxidation with blue triangles. (a) Comparison between the XPS peaks of Si 2p, before and after the etching process and after 300 h of oxidation in air. It is possible to note how the chemical etching reduces the amount of oxides, inducing changes in the peak shape. (b) Effects of the variation of the oxide layer thickness on the I – V characteristics.

peaks before (pink filled circles), immediately after (black filled diamonds), and 300 h after (blue filled triangle) the etching process are shown. It is easy to notice how the etching process acts on the oxide layer, removing the SiO_x and reducing the amount of SiO₂, inducing a change in the overall Si2p shape. When the sample is left in air for 300 h, the SiO_x contribution did not show any detectable increase, while an oxidation of Si to SiO₂ is clearly observed.

The combined effect of the etching and oxidation processes on the device operation is evident in Figure 6b, where the I – V curves for all the three steps are shown. Before the etching, sample B was the one with the lowest efficiency and its I – V characteristic is shown in Figure 6b (pink circles). After the oxide layer is removed through the etching process, the values of the electric parameters (V_{OC} and I_{SC}) decrease significantly and the cell performance deteriorates considerably (black diamonds). However, from the very first hours after the etching, an improvement of the I – V curve is observed, till the cell reaches a stable behavior after a few tens of hours, staying constant up to 300 h (blue triangle).

These results also demonstrate that the oxide layers, as well as the CNT film, should have an optimal thickness, necessary to achieve high efficiencies. It is important to note that the change induced in the cell is effective, stable, and durable, disclosing the possibility to regenerate cells subjected for over one year to oxidation in air. It is important to remark that while the SiO₂

contribution increases, the SiO_x contribution does not show appreciable change up to 300 h after the etching, suggesting that SiO_x can be ascribed to one of the processing steps in the cell assembling. In this frame, SiO_x appears to be detrimental for the cell efficiency, confirming the correlation observed in Table 3 between the SiO_x/SiO₂ thickness ratio and the cell efficiency.

With regard to the overall cell efficiency, we do not exclude that the optimal situation could be found in a suitable ratio between the thickness of the CNT film and of the SiO₂ layer, as the proper thickness of the SiO₂ layer may itself depend on the CNT thickness. This issue is being systematically checked on a much larger set of samples.

CONCLUSION

AR-XPS allowed us to carry-out a nondestructive profiling of a complex interface at the basis of a hybrid CNT/Si PV heterojunction. We have been able to directly probe that a chemically heterogeneous Si–O layer exists between the bulk Si n-type side of the junction and the p-type CNT layer. This layer is composed of SiO₂ and SiO_x, with a thickness in the 2–3 nm range. This proves and properly addresses early claims about the existence and the role of the silicon oxide in the PV cell.¹⁷ The effects of the Si–O layer on the junction efficiency are tracked by etching the junction in HF and collecting XPS and I – V curves as the native oxide layer builds up. We show that etching removes the SiO_x layer and that the efficiency improves when a SiO₂ layer has regrown, due to spontaneous oxidation in air. Therefore, unlike that previously believed,³⁵ SiO_x is detrimental for the PV cell operation, while SiO₂ acts as a buffer layer that improves the PV cell performances. Within the resolution of our XPS probe, HF etching does not appear to affect the CNT local electronic properties, excluding chemical doping of CNTs as the leading effect in the efficiency recovery after etching.

In the present study, the silicon oxide buffer layer could be accessed by XPS provided that the CNT film thickness was not too high. This limited our choice to samples with a thickness of the CNT layers below about 40 nm. For several reasons, the efficiency of these cells is not high as compared to other samples reported in the literature. As first, the best performing cells we prepared with the present technique are those fabricated with 4–5 mL of CNT dispersion. Second, comparison must be performed with devices like the present ones without any particular treatment (further p-type doping of CNTs and/or acid treatments), which have been reported to have efficiencies between 5% and 7% (see, e.g., ref 14). With respect to these devices, all our samples are characterized by a lower short circuit current density (J_{sc}) and fill factor (FF), thus yielding lower efficiencies. Both the low J_{sc} and FF values can be ascribed to too high series resistance, probably originating (1) from the presence of residual SDS surfactant (visible in the XPS spectrum through Na and S peaks), which, being an insulator, can increase the CNT film resistance, and, at a lower extent, (2) from the choice of a relatively high series resistance for the wafer. Finally, the contacts electrodes, based on silver paste, can be at the origin of additional resistances. Despite these limitations, the etching treatment yields a remarkable improvement of the fill factor (from 22% before etching to 36%, measured 300 h after the etching) and ultimately on the efficiency (from 0.2% to 0.35%) even in the low-efficiency cell (i.e., sample B), disclosing similar improvements for the best performing devices.

■ ASSOCIATED CONTENT

■ Supporting Information

Optical characterization of CNT thin layers and calculation of the XPS intensity of carbon and silicon core levels at different takeoff and acceptance angles of the analyzer. This information is available free of charge via the Internet at <http://pubs.acs.org>

■ AUTHOR INFORMATION

Corresponding Author

*Phone: ++39-030-2406716; e-mail: sangalet@dmf.unicatt.it.

Notes

The authors declare no competing financial interest.

■ ACKNOWLEDGMENTS

The Roma Tor Vergata group acknowledges the financial support of the European Office of Aerospace Research and Development (EOARD) through Air Force Office of Scientific Research Material Command, USAF, under Grant No. FA8655-11-1-3036.

■ REFERENCES

- (1) *Carbon Nanotubes*; Reich, S.; Thomsen, C.; Maultzsch, J., Eds.; Wiley-VHC: New York, 2004.
- (2) Minami, N.; Kazaoui, S.; Jacquemin, R.; Yamawaki, H.; Aoki, K.; Kataura, H.; Achiba, Y. Optical Properties of Semiconducting and Metallic Single Wall Carbon Nanotubes: Effects of Doping and High Pressure. *Synth. Met.* **2001**, *116*, 405–409.
- (3) Castrucci, P.; Scilletta, C.; Del Gobbo, S.; Scarselli, M.; Camilli, L.; Simeoni, M.; Delley, B.; Continenza, A.; De Crescenzi, M. Light Harvesting with Multiwall Carbon Nanotube/Silicon Heterojunctions. *Nanotechnology* **2011**, *22*, 115701–115709.
- (4) Misewich, J. A.; Martel, R.; Avouris, P.; Tsang, J. C.; Heinze, S.; Tersoff, J. Electrically Induced Optical Emission from a Carbon Nanotube FET. *Science* **2003**, *300*, 783–786.
- (5) Barazzouk, S.; Hotchandani, S.; Vinodgopal, K.; Kamat, P. V. Single Wall Carbon Nanotube Films for Photocurrent Generation. A Prompt Response to Visible Light Irradiation. *J. Phys. Chem. B* **2004**, *108*, 17015–17018.
- (6) Castrucci, P.; Tombolini, F.; Scarselli, M.; Speiser, E.; Del Gobbo, S.; Richter, W.; De Crescenzi, M.; Diociaiuti, M.; Gatto, E.; Venanzi, M. Large Photocurrent Generation in Multiwall Carbon Nanotubes. *Appl. Phys. Lett.* **2006**, *89*, 253107–253109.
- (7) Scarselli, M.; Castrucci, P.; De Crescenzi, M. Electronic and Optoelectronic Nano-Devices Based on Carbon Nanotubes. *J. Phys.: Condensed Matter* **2012**, *24*, 313202–313238.
- (8) Landi, B. J.; Raffaele, R. P.; Castro, S. L.; Bailey, S. G. Single-Wall Carbon Nanotube–Polymer Solar Cells. *Prog. Photovolt: Res. Appl.* **2005**, *13*, 1–8.
- (9) Kymakis, E.; Amaratunga, G. A. Single-Wall Carbon Nanotube/Conjugated Polymer Photovoltaic Devices. *Appl. Phys. Lett.* **2002**, *80*, 112–114.
- (10) Rowell, M. W.; Topinka, M. A.; McGehee, M. D.; Prall, H.-J.; Dennler, G.; Sariciftci, N. S.; Hu, L.; Gruner, G. Organic Solar Cells with Carbon Nanotube Network Electrodes. *Appl. Phys. Lett.* **2006**, *88*, 233506–233508.
- (11) van de Lagemaat, J.; Barnes, T. M.; Rumbles, G.; Shaheen, S. E.; Coutts, T. J.; Weeks, C.; Levitsky, I.; Peltola, J.; Glatkowski, P. Organic Solar Cells with Carbon Nanotubes Replacing In₂O₃:Sn as the Transparent Electrode. *Appl. Phys. Lett.* **2006**, *88*, 233503–233505.
- (12) Jia, Y.; Wei, J.; Wang, K.; Cao, A.; Shu, Q.; Gui, X.; Zhu, Y.; Zhuang, D.; Zhang, G.; Ma, B.; et al. Nanotube-Silicon Heterojunction Solar Cells. *Adv. Mater.* **2008**, *20*, 4594–4598.
- (13) Jung, Y.; Li, X.; Rjan, N. K.; Taylor, A. D.; Reed, M. A. Record High Efficiency Single-Walled Carbon Nanotube/Silicon p-n Junction Solar Cells. *Nano Lett.* **2013**, *13*, 95–99.
- (14) Jia, Y.; Cao, A.; Bai, X.; Li, Z.; Zhang, L.; Guo, N.; Wei, J.; Wang, K.; Zhu, H.; Wu, D.; et al. Achieving High Efficiency Silicon-Carbon Nanotube Heterojunction Solar Cells by Acid Doping. *Nano Lett.* **2011**, *11*, 1901–1905.
- (15) Le Borgne, V.; Gautier, L. A.; Castrucci, P.; Del Gobbo, S.; De Crescenzi, M.; El Khakani, M. A. Enhanced UV Photoresponse of KrF-Laser-Synthesized Single-Wall Carbon Nanotubes/n-Silicon Hybrid Photovoltaic Devices. *Nanotechnology* **2012**, *23*, 215206–215216.
- (16) Hao, F.; Dong, P.; Zhang, J.; Zhang, Y.; Loya, P. E.; Hauge, R. H.; Li, J.; Lou, J.; Lin, H. High Electrocatalytic Activity of Vertically Aligned Single-Walled Carbon Nanotubes towards Sulfide Redox Shuttles. *Sci. Rep.* **2012**, *2*, 368–374.
- (17) Jia, Y.; Cao, A.; Kang, F.; Li, P.; Gui, X.; Zhang, L.; Shi, E.; Wei, J.; Wang, K.; Zhu, H.; et al. Strong and Reversible Modulation of Carbon Nanotube–Silicon Heterojunction Solar Cells by an Interfacial Oxide Layer. *Phys. Chem. Chem. Phys.* **2012**, *14*, 8391–8396.
- (18) Seah, M. P.; Gilmore, I.; Beamson, G. XPS: Binding Energy Calibration of Electron Spectrometers 5 - Re-evaluation of the Reference Energies. *Surf. Interface Anal.* **1998**, *26*, 642–649.
- (19) Waligorski, G.; Cooke, W. E. Measuring Angular Distributions with Large-Acceptance-Angle Detectors. *Meas. Sci. Technol.* **2001**, *12*, 299–305.
- (20) Aarnik, W. A. M.; Weishaupt, A.; van Silfout, A. Angle-Resolved X-ray Photoelectron Spectroscopy (ARXPS) and a Modified Levenberg-Marquardt Fit Procedure: a New Combination for Modeling Thin Layers. *Appl. Surf. Sci.* **1990**, *45*, 37–48.
- (21) Yeh, J. J.; Lindau, I. Atomic Subshell Photoionization Cross Sections and Asymmetry Parameters: $1 \leq Z \leq 103$. *Atomic Data Nuclear Data Tables* **1985**, *32*, 1–155.
- (22) Werner, W. S. M. Electron Transport in Solids for Quantitative Surface Analysis. *Surf. Int. Anal.* **2001**, *31*, 141–176.
- (23) Tilinin, I.; Jablonski, A.; Zemek, J.; Hucek, S. J. Escape Probability of Signal Photoelectrons from Non Crystalline Solids: Exact Solution in the Transport Approximation. *J. Electron Spectrosc. Relat. Phenom.* **1997**, *97*, 127–140.
- (24) Jablonski, A. Transport Cross Section for Electrons at Energies of Surface-Sensitive Spectroscopies. *Phys. Rev. B* **1998**, *58*, 16470–16480.
- (25) Doniach, S.; Sunjic, M. Many-Electron Singularity in X-ray Photoemission and X-ray Line Spectra from Metals. *J. Phys. C: Solid State Phys.* **1970**, *3*, 285–291.
- (26) Hüfner, S. *Photoelectron Spectroscopy: Principles and Applications*; Springer: Berlin, 1995.
- (27) Sette, F.; Wertheim, G.; Ma, Y.; Meigs, G.; Modesti, S.; Chen, C. Lifetime and Screening of the C 1s Photoemission in Graphite. *Phys. Rev. B* **1990**, *41*, 9766–9770.
- (28) Wepasnick, K. A.; Smith, B. A.; Bitter, J. L.; Fairbrother, D. H. Chemical and Structural Characterization of Carbon Nanotube Surfaces. *Anal. Bioanal. Chem.* **2010**, *396*, 1003–1014.
- (29) Aoyama, T.; Sugii, T.; Ito, T. Determination of Band Line-up in β -SiC/Si Heterojunction for Si-HBT's. *Appl. Surf. Sci.* **1989**, *41*, 584–586.
- (30) Galuska, A.; Uht, J.; Marquez, N. Reactive and Nonreactive Ion Mixing of Ti Films on Carbon Substrates. *J. Vac. Sci. Technol. A* **1988**, *6*, 110–122.
- (31) Maruyama, T.; Bang, H.; Fujita, N.; Kawamura, Y.; Naritsuka, S.; Kusunoki, M. STM and XPS Studies of Early Stages of Carbon Nanotube Growth by Surface Decomposition of 6H-SiC(000–1) Under Various Oxygen Pressures. *Diamond Relat. Mater.* **2007**, *16*, 1078–1081.
- (32) Liu, Y.; Zhang, Z.; Wells, M. C.; Beebe, T. P. Growth and Reactions of SiO_x/Si Nanostructures on Surface-Templated Molecule Corals. *Langmuir* **2005**, *21*, 8883–8891.
- (33) Wei, H.; Kim, S. N.; Kim, S.; Huey, B. D.; Papadimitrakopoulos, F.; Marcu, H. L. Site-Specific Forest-Assembly of Single-Wall Carbon Nanotubes on Electron-Beam Patterned SiO_x/Si Substrates. *Mater. Sci. Eng. C* **2008**, *28*, 1366–1371.
- (34) Le Borgne, V.; Castrucci, P.; Del Gobbo, S.; Scarselli, M.; De Crescenzi, M.; Mohamedi, M.; El Khakani, M. A. Enhanced

Photocurrent Generation from UV-Laser-Synthesized-Single-Wall-Carbon-Nanotubes/n-Silicon Hybrid Planar Devices. *Appl. Phys. Lett.* **2010**, 97, 193105–193107.

(35) Jia, Y.; Li, P.; Gui, X.; Wei, J.; Wang, K.; Zhu, H.; Wu, D.; Zhang, L.; Cao, A.; Xu, Y. Encapsulated Carbon Nanotube-Oxide-Silicon Solar Cells With Stable 10% Efficiency. *Appl. Phys. Lett.* **2011**, 98, 133115–133118.